Cobalt nanoparticles encapsulated in porous nitrogen-doped carbon: Oxygen activation and efficient catalytic removal of formaldehyde at room temperature

Dandan Zhu[a,b], Yu Huang[b,c,*], Jun-ji Cao[b,c], Shun Cheng Lee[d], Meijuan Chen[e], Zhenxing Shen[a,b,*]

[a] Department of Environmental Sciences and Engineering, Xi'an Jiaotong University, Xi'an, 710049, China
[b] Key Lab of Aerosol Chemistry & Physics, SKLLQG, Institute of Earth Environment, Chinese Academy of Sciences, Xi'an, 710049, China
[c] CAS Center for Excellence in Quaternary Science and Global Change, Xi'an, 710061, China
[d] Department of Civil and Environmental Engineering, The Hong Kong Polytechnic University, Hong Kong, China
[e] School of Human Settlements and Civil Engineering, Xi'an Jiaotong University, Xi'an, 710049, China

ARTICLE INFO

ABSTRACT

The removal of carcinogenic formaldehyde (HCHO) to improve indoor air quality has attracted significant attention. Designing efficient catalysts for practical HCHO oxidation without use of noble metals remains challenging. In this study, metallic Co nanoparticles were encapsulated with porous nitrogen-doped carbon (Co@NC). This catalyst achieved HCHO elimination at room temperature for the first time. The as-prepared Co@NC catalyst exhibited superior catalytic activity (> 80%) for HCHO removal compared with the oxidized one, and possessed the excellent stability. Theoretical calculations showed that the metallic Co in Co@NC is the active site for O_2 dissociation, which enhanced the catalytic activity compared to traditional transition-metal oxides, such as Co_3O_4 with the high-valence state Co^{3+} providing active sites. The formate species was the main intermediate, which was further oxidized to CO_2 as the final product. Hence, an efficient non-noble-metal catalyst for room-temperature HCHO oxidation was developed.

1. Introduction

Formaldehyde (HCHO) is a prevalent indoor air pollutant and has been recognized as a carcinogenic compound [1–3]. Since long-term exposure to HCHO has severe adverse effects on human health and most people spend the majority of the day indoors, there is a strong motivation to reduce indoor HCHO levels to improve indoor air quality [4]. Various approaches, including adsorption [5,6], photocatalytic oxidation [3,7,8], plasma techniques [9], and thermal catalytic oxidation [10], have been investigated for volatile organic compounds (VOCs) and HCHO removal. Thermocatalysis is a particularly promising technique because it completely oxidizes HCHO into harmless CO_2 and H_2O using suitable catalysts with high activity, long-term stability, and reusability [11–13]. Although supported noble metals catalysts such as Pt/MnO_x-CeO_2 [11] and Pt/TiO_2 [14] have shown 100% HCHO conversion at room temperature, the scarcity and high cost of noble metals inhibited their practical applications in indoor air purification. The cheap and plentiful transition-metal oxides have also been widely investigated for HCHO oxidation [15–22]. In particular, spinel-type

Co_3O_4 has been extensively investigated due to its versatile redox properties and high stability [15,18,21]. The catalytic activity of HCHO oxidation over Co_3O_4 catalysts reported in literatures was listed in Table S1. However, only 20.3% of HCHO was converted into CO_2 at 25 °C over Co_3O_4 [23]. Therefore, development of a cost-efficient catalyst exhibiting superior catalytic performance at room temperature is necessary to realize effective HCHO removal.

Generally, catalytic oxidation of HCHO using Co_3O_4-based catalysts follows the Mars–Van Krevelen mechanism, in which O_2 activation and the amounts of reactive oxygen species play significant roles [15,18]. In addition, the number of active sites affects the catalytic activity [15]. In general, metal ions with high valence states, such as Co^{3+}, are thought to be the active sites in transition-metal oxides [15,21,23,24]. However, the activation ability of transition-metal cations is relatively low, resulting in poor catalytic activity at ambient temperature. In contrast, noble metal nanoparticles (NPs) such as Pt^0 can behave as excellent active sites with strong ability to activate O−O bonds [25]. This inspired investigation of the dissociation of O_2 on metallic Co, and the resulting HCHO catalytic-oxidation activity were encouraging to be

investigated. Although Co^0 NPs have shown excellent capability as heterogeneous catalysts [26,27], the catalytic oxidation of VOCs has rarely been reported due to easy oxidation of metallic Co NPs at relatively high temperature ($> 200\,°C$). Therefore, it is of great interest to explore the catalytic capability of metallic Co NPs for HCHO oxidation at room temperature.

Metal–organic frameworks (MOFs) containing Co^{2+} have been used to fabricate metallic Co/carbon composites via pyrolysis in an inert atmosphere [27]. Using this method, the porous carbon formed from organic ligands can isolate the Co NPs and prevent them from agglomerating, while also acting as an appropriate support to adsorb and concentrate the target reactants during heterogeneous catalysis. In addition, the excellent electrical conductivity of carbon materials can promote electron transport in metal/carbon composites, which may facilitate the catalytic oxidation reaction [28]. Notably, the nitrogen-containing ligands of MOF can be used as an effective nitrogen source to produce nitrogen-doped carbon; basic pyridinic nitrogen sites can promote the adsorption of acidic HCHO [29,30]. Therefore, we hypothesized that Co NPs embedded in nitrogen-doped carbon derived from a nitrogen-containing MOF could be a superior catalyst for HCHO degradation.

In this study, we investigated O_2 dissociation on metallic Co NPs by theoretical calculations, and experimentally investigated the HCHO catalytic-oxidation activity at room temperature using metallic Co NPs encapsulated in a porous nitrogen-doped carbon (Co@NC) derived from a nitrogen-containing Co-MOF (ZIF-67) through one-step calcination in a nitrogen atmosphere. ZIF-67 was firstly synthesized as previously reported [31], and then was pyrolyzed in a nitrogen atmosphere. Considering that Co_3O_4 has been extensively investigated for HCHO oxidation, it is meaningful to compare the catalytic activity of metallic Co and Co_3O_4-based catalysts in HCHO oxidation. Therefore, the as-prepared Co@NC was subsequently oxidized to convert Co into Co_3O_4, in order to partially coat Co with a Co_3O_4 layer. Comprehensive characterizations were conducted to understand the differences in the structures and compositions of the as-prepared and oxidized samples. Co^0 was identified as the active site for O_2 dissociation, and a plausible reaction mechanism for HCHO degradation is proposed here.

2. Experimental

2.1. Catalyst preparation

All chemicals used were analytical reagent and used as received without any further purification. 2-methylimidazole (2-mIm) was purchased from Aladdin Industrial Corporation. Other reagents were bought from Sinopharm Chemical Reagent Co., Ltd.. Water with a resistivity exceeding $18\,MΩ\,cm$ was obtained using a Millipore system.

Before preparation of cobalt-based catalysts, the precursor ZIF-67 was synthesized initially according to a previously reported procedure [31]. Typically, 1.16412 g of $Co(NO_3)_2 \cdot 6H_2O$ and 1.3136 g of 2-mIm were dissolved in 50 mL methanol, respectively, to obtain the corresponding methanolic solutions, which were then rapidly mixed with each other under continuous stirring, followed by vigorous stirring for 10 min and undisturbed aging for 24 h at room temperature. The purple powders were collected by centrifugation, washing with ethanol for 3 times, and drying overnight at $80\,°C$ in an vacuum oven. Co@NC was obtained through pyrolysis of ZIF-67 at $600\,°C$ for 2 h in a nitrogen atmosphere with a heating rate of $2\,°C\,min^{-1}$ in a tubular furnace. A schematic illustration of the preparation of Co@NC by pyrolysis is shown in Scheme S1. Then, the as-prepared Co@NC was treated at $150\,°C$ in air atmosphere to oxidize metallic Co by varying oxidizing duration, resulting in the carbon encapsulated Co-Co_3O_4 with different oxidation degree of Co, and referring as Co-Co_3O_4@NC-t ($t = 30$ or 60 h). In addition, the porous carbon (NC) after removal of metallic Co from Co@NC was obtained by acid-leaching with aqua regia for several times, followed by centrifuging, washing, and drying in an vacuum

oven. To elucidate the contribution of NC for HCHO removal, the carbon encapsulated and un-encapsulated Co_3O_4 catalysts were prepared through thermal treating ZIF-67 precursor by adjusting the preparation conditions. Specifically, the carbon encapsulated Co_3O_4 (Co_3O_4@NC) was prepared by oxidizing the as-prepared Co@NC at $250\,°C$ in air; while the un-encapsulated Co_3O_4 (Co_3O_4) was obtained by thermally treating Co@NC at $550\,°C$ in air to remove the carbonaceous species thoroughly.

2.2. Physicochemical characterization

X-ray diffraction (XRD) patterns were measured on a X'pert Pro powder diffractometer (PANalytical Corp., the Netherlands) using Cu Kα radiation ($λ = 0.15406\,nm$) at a scan rate of $0.017°\cdot min^{-1}$. Scanning electron microscopy (SEM) analyses were performed on a JSM-6700F microscope (JEOL Corp., Japan) equipped with a energy dispersive X-ray spectroscopy (EDS). Transmission electron microscopy (TEM) and high-resolution TEM (HRTEM) images were obtained using a FEI Tecnai G2 F20 transmission electron microscope (FEI Corp., Japan) with acceleration voltage of 200 kV. X-ray photoelectron spectroscopy (XPS) was carried out on an Escalab 250 Xi spectrometer (Thermo Scientific, USA) with binding energies calibrated using the C 1s peak at 284.6 eV as a reference. Raman spectra were recorded on a DXR Raman Microscope (Thermo Fisher Scientific, USA) using a 532-nm argon laser. N_2 sorption experiments were conducted at 77 K on an accelerated surface area and porosimetry analyzer (ASAP 2020 Plus HD88, Micromeritics Instrument Corp., USA). The specific surface areas and pore size distributions were determined based on the Brunauer–Emmett–Teller (BET) and nonlinear density functional theory (DFT) methods using adsorption data of N_2. Prior to N_2 adsorption measurements, all samples were evacuated for 12 h at $150\,°C$ under high vacuum. Thermogravimetric analysis (TGA; STA 449 F5, Netzsch, Germany) was performed at a heating rate of $5\,°C\,min^{-1}$ in air atmosphere. in situ diffuse reflectance infrared Fourier transform (DRIFT) spectra were obtained on a VERTEX 70 FTIR spectrometer (Bruker, German). The catalyst diluted by KBr was firstly pretreated with a gas flow of He at $150\,°C$ for 30 min. The background spectrum was obtained after the reactor cell cooled to room temperature. Afterwards, the gas flow was changed to the reaction gas (50 ppm HCHO) to record the spectra at a flow rate of $100\,mL\cdot min^{-1}$ (O_2 20 vol.%, N_2 balance).

2.3. Catalytic activity testing

The catalytic activity of different catalysts for HCHO oxidation was evaluated in a fixed-bed reactor under atmospheric pressure at room temperature ($25 ± 2\,°C$). For each test, 0.075 g of catalyst (40–60 meshes) was loaded in a stainless-steel tube with a internal diameter of 6 mm. Gaseous HCHO was produced by passing a purified air flow through the formalin solution in the stainless steel container kept at $15\,°C$ by a low-temperature cold trough. The initial reactant mixture consisted of 100 ppm HCHO in Air, with the total flow rate controlled at $100\,mL\cdot min^{-1}$ by mass-flow meters, affording a gas hourly space velocity (GHSV) of $80,000\,mL\cdot g^{-1}\,h^{-1}$. The real-time concentration of HCHO and CO_2 from outlet of the reactor was monitored by a INNOVA 1412i photoacoustic gas monitor with detection limit of 0.04 ppm for HCHO, and 5.1 ppm for CO_2 (LumaSense Technologies, Inc., Denmark). The HCHO removal efficiency ($η$) and conversion rate (X) were determined according to the following equations (Eqs. (1) and (2)) [32,33]:

$$η\,(\%) = \left(1 - \frac{C_t}{C_0}\right) \times 100\% \tag{1}$$

$$X\,(\%) = \frac{\Delta CO_2}{C_0} \times 100\% \tag{2}$$

where C_t and C_0 represent the HCHO outlet concentration at a given

time and the inlet concentration (ppm), respectively; $\triangle CO_2$ is the generated amount (ppm) of CO_2 during HCHO removal. The recycling runs for HCHO removal was conducted by sweeping the used catalysts with purified air at room temperature before the next test.

2.4. Theoretical calculations

All spin-polarized DFT calculations were performed using the Cambridge Sequential Total Energy Package in Material Studio 8.0, in which the electron-ion interactions were expressed by projector-augmented wave method. The generalized gradient approximation proposed by Perdew-Burke-Ernzerhof functional was used to describe the exchange-correlation energies and potential. For geometry optimization, a large convergence of the plane wave expansion was obtained with an energy cut off of 380 eV; the Brillouin zone was sampled in a $2 \times 2 \times 1$ Monkhorst-Pack set. The geometries were not optimized, until the energy, the force and the max displacement converge to 2.0×10^{-5} eV/atom, 0.05 eV/Å, and 2×10^{-3} Å, respectively.

For a reaction such as R (reactant) → P (product) on catalyst surface, the activation barrier (E_a) and reaction energy (ΔH) are calculated according to the following formulas:

$$Ea = E_{TS} - E_R \tag{3}$$

$$\Delta H = E_P - E_R \tag{4}$$

where E_R and E_P are the total energies of the adsorbed reactant and product, respectively, and E_{TS} is the total energies of the transition state (TS).

3. Results and discussion

3.1. Catalyst characterization

The morphology and crystallinity of the ZIF-67 precursor were examined using SEM and XRD, respectively. Fig. S1a shows that ZIF-67 has a rhombic dodecahedron structure with a size of 300–400 nm. XRD spectra (Fig. S1b) showed that the diffraction peaks of the as-synthesized ZIF-67 were in good agreement with simulated ones, confirming that both the purity and crystallinity of ZIF-67 were very high. Subsequently, ZIF-67 was thermally treated to obtain the carbon encapsulated cobalt-based catalysts. The crystallinity and phase structures of Co@NC and Co-Co_3O_4@NC were identified by XRD patterns (Fig. 1a). Peaks at 2θ = 44.2°, 51.5°, and 75.9° in Co@NC were indexed to (111), (200), and (220) reflections of face-centered-cubic (FCC) phase of cobalt (JCPDS No. 15-0806), respectively, while the weak and broadened peak at ~26° was assigned to the (002) lattice plane of carbon, confirming that Co^{2+} and the organic ligands in ZIF-67 were transformed into metallic Co and carbon, respectively, after pyrolysis in nitrogen [34]. The average crystallite size of metallic Co was 7.8 nm, determined using Scherrer's equation and the (111) peak. For Co-Co_3O_4@NC-30 obtained after oxidation of Co@NC, the intensity of metallic Co peaks decreased significantly, accompanied by the emergence of a new peak at 36.8°, which was assigned to the (311) crystal plane of cubic Co_3O_4 (JCPDS No. 42-1467) due to the partial oxidation of Co in Co@NC under mild air oxidation for 30 h [35]. The XRD peaks of Co-Co_3O_4@NC-60 were similar to those of Co-Co_3O_4@NC-30; further decrease in the metallic Co peak intensity after prolonged oxidation indicated that the degree of oxidation of metallic Co could be controlled by changing the heat-treatment time.

Raman spectra (Fig. 1b) showed the characteristic peaks of graphitic carbon at 1326 cm^{-1} (D band) and 1586 cm^{-1} (G band) [36]. The relatively high I_D/I_G ratio (~1) calculated from the peak intensities of the D and G bands indicated a low degree of graphitization of the carbon materials, consistent with the XRD results showing weak graphite carbon peaks. The I_D/I_G ratios of Co@NC and Co-Co_3O_4@NC were very similar, indicating similar graphitic structures. Hence, the mild

oxidation conditions did not significantly affect the degree of graphitization. The morphology of the as-prepared Co@NC (Fig. 1c) was similar to that of ZIF-67, although the size decreased slightly and the surface roughened due to gas evolution during decomposition of the organic ligands. The elemental distribution of Co@NC determined using EDS (Fig. 1d) identified Co, C, N, and O co-existing in Co@NC, where similar results were observed for Co-Co_3O_4@NC-30 (Fig. S2). Elemental maps (Fig. 1e) confirmed that all elements were distributed uniformly in Co@NC.

TEM measurements were used to investigate the particle-size distributions and phase compositions of the Co-based catalysts. Fig. 2a shows that Co@NC was comprised of nanoscale Co particles embedded in the porous carbon. The Co NPs had a size range of 4–11 nm and average diameter of 7.4 nm, consistent with the XRD data. HRTEM image in Fig. 2b shows that Co particles were isolated and surrounded by graphitic carbon. The corresponding enlarged image (Fig. 2c) shows evident lattice fringes with interplanar distances of 0.203 and 0.340 nm, which were ascribed to the (111) and (002) crystal planes of metallic Co and graphitic carbon, respectively [26]. Co-Co_3O_4@NC-30 showed a similar particle distribution (4–12 nm) as that of Co@NC (Fig. 2d and Fig. S3), while a new phase with a thickness of about 2 nm was observed between the Co particles and graphitic carbon (Fig. 2e). The clear lattice fringes with d-spacings of 0.206, 0.246, and 0.340 nm (Fig. 2f) were indexed to the (111), (311), and (002) crystal planes of metallic Co, spinel Co_3O_4, and graphitic carbon, respectively, implying that metallic Co was partially converted to Co_3O_4 via the mild oxidation [37].

The surface compositions and chemical states of the Co-based catalysts were investigated by XPS. Survey spectra in Fig. 3a identified the presence of Co, C, N, and O in all catalysts, where an increase in the intensity of the O 1s peak was observed for Co-Co_3O_4@NC. The atomic fractions of these four elements measured by XPS are listed in Table 1, further confirming the oxidation of Co. Fig. 3b shows high-resolution Co 2p spectra of Co@NC and Co-Co_3O_4@NC. The peaks centered at 778.7 and 793.8 eV were attributed to Co^0, while the other peaks at 780.9 and 796.4 eV were assigned to Co^{2+} in CoO, which originated from surface oxidation of Co^0 in air [38]. Notably, the peaks assigned to Co^0 increased significantly after Ar^+ sputtering, while the signals from Co^{2+} gradually weakened over the sputtering time, indicating Co^0 was the main Co species in Co@NC (Fig. S4). The peaks at 786.2 and 803.4 eV were satellite peaks [35]. In comparison with Co@NC, two pairs of peaks ($2p_{3/2}/2p_{1/2}$) at 780.3/795.4 eV and 782.0/797.5 eV assigned to the Co^{3+} and Co^{2+} in Co_3O_4 [39,40] were observed in the spectrum of Co-Co_3O_4@NC-30, while no Co^0 signals were observed, which is explained by Co_3O_4 covering metallic Co and the limited sensitivity of the XPS technique. However, the peaks assigned to Co^0 could be clearly observed after Ar^+ sputtering for 60 s (Fig. S5). In the O 1s spectrum of Co@NC (Fig. 3c), two peaks at 531.5 and 533.2 eV were assigned to C=O in the carbon support and adsorbed water molecules, respectively [26,34]. In addition, an additional peak at 530.1 eV was clearly observed in Co-Co_3O_4@NC-30, which was ascribed to Co–O bonds in Co_3O_4 [26]. The C 1s and N 1s spectra of Co@NC are shown in Fig. 3d, where the C 1s peaks were deconvoluted into three peaks at 284.8, 285.9, and 288.7 eV, corresponding to the sp^2-hybridized C=C, C–N/C–O, and C=O bonds, respectively [26]. The peaks at 398.8, 400.0, and 401.0 eV in the N 1s spectrum were ascribed to pyridinic N, pyrrolic N, and graphitic N, respectively [34,41,42]. The C 1s and N 1s spectra of Co-Co_3O_4@NC-30 (Fig. S6) were similar to that of Co@NC. These results further confirmed that metallic Co in Co@NC was partially transformed into Co_3O_4 after successive oxidization, with little variation in the carbonaceous species. The oxidation of metallic Co and corresponding variation in the structures and chemical compositions is expected to significantly affect the catalytic activity.

Given that the textural properties of the catalysts are of vital importance for the catalytic oxidation reaction, N_2 adsorption–desorption experiments were performed to evaluate the surface area and pore
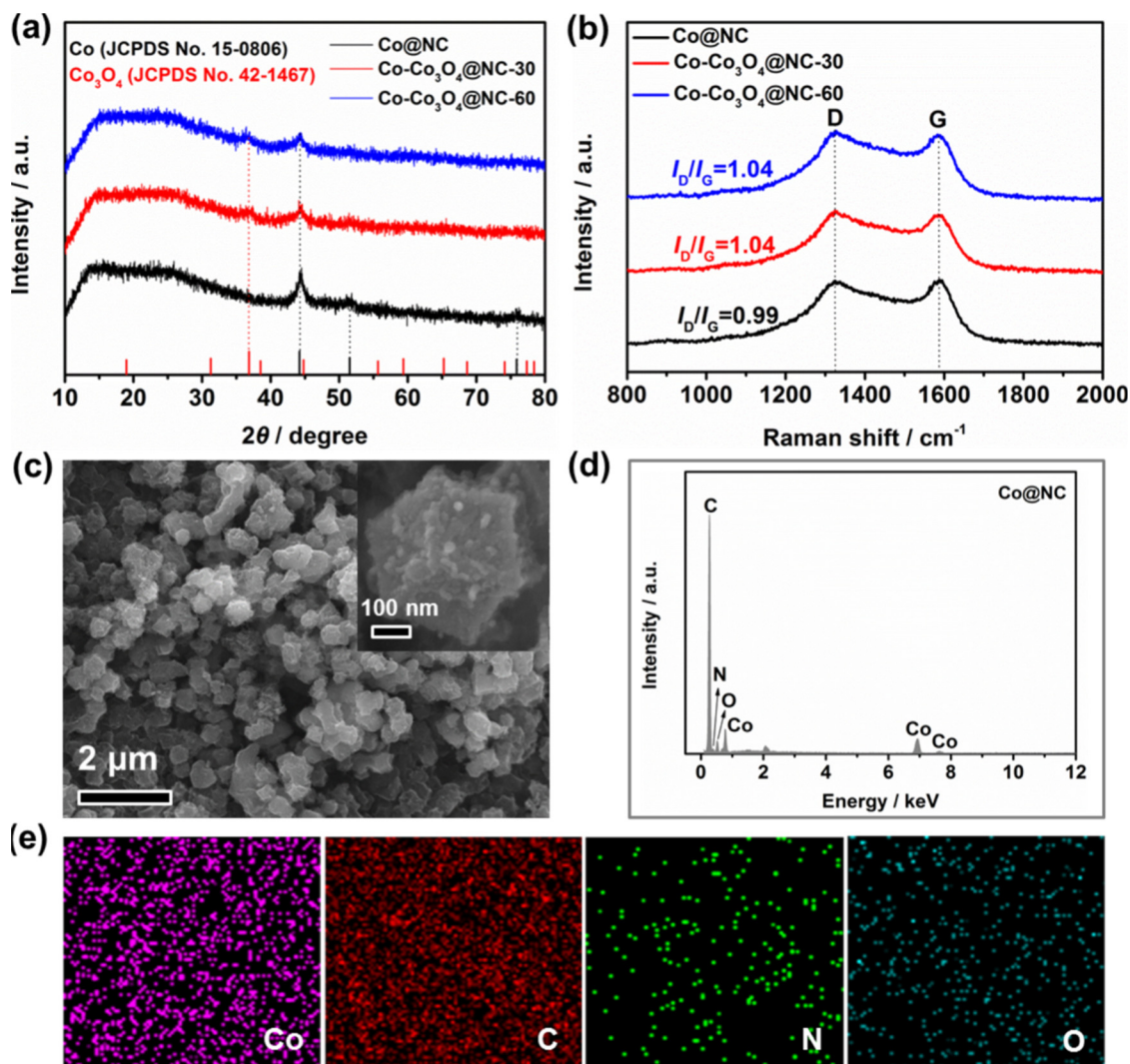
Fig. 1. (a) XRD patterns and (b) Raman spectra of Co@NC, Co-Co$_3$O$_4$@NC-30, and Co-Co$_3$O$_4$@NC-60. (c) SEM images and (d) EDS spectrum of Co@NC. (e) Element maps of Co, C, N, and O in Co@NC.

structure of Co@NC and Co-Co$_3$O$_4$@NC-30. These Co-based catalysts showed typical type-II isotherms with a type H3 loop (Fig. S7a) [43]. Specifically, the sharp increase in adsorbed volume at low relative pressure indicates the presence of micropores, while the gradual increase in the absorbed volume at medium relative pressure with hysteresis loops ($0.4 < P/P_0 < 1.0$), and the increase in absorbed volume at high pressure implies the presence of mesopores and macropores, respectively. Notably, Co@NC showed better adsorption capability than Co-Co$_3$O$_4$@NC-30. As shown in Table 2, both the BET surface area and pore volume of Co@NC were larger than those of Co-Co$_3$O$_4$@NC-30. The pore-width distribution curves in Fig. S7b showed that both Co@NC and Co-Co$_3$O$_4$@NC-30 contained many micropores and mesopores, as well as some macropores, consistent with the N$_2$ sorption isotherms. Such hierarchical porous structures are beneficial for adsorption, diffusion, and subsequent conversion of the gaseous reactants [44,45]. It was expected that the high surface area, large pore volume, and hierarchical porous structure would facilitate HCHO oxidation.

3.2. Catalytic activity for HCHO removal

The catalytic activity of Co@NC and Co-Co$_3$O$_4$@NC for HCHO elimination was evaluated using a fixed-bed reactor with an initial HCHO concentration of 100 ppm at room temperature. Co@NC clearly showed excellent HCHO removal behavior (Fig. 4a) and achieved >

85% removal (calculated using Eq. (1)) with minimal deactivation observed over the 60 min testing time. However, using Co-Co$_3$O$_4$@NC-30, deactivation occurred, although 80% of the initial HCHO was eliminated initially. This distinct difference in HCHO removal efficiency showed that the mild oxidizing treatment of Co@NC adversely affected HCHO removal. To elucidate the reasons for this, the contribution of the surface properties to HCHO removal was evaluated. The content of pyridinic N in Co@NC was slightly higher than that in Co-Co$_3$O$_4$@NC-30 (Table 1), suggesting that Co@NC could show stronger adsorption of HCHO as the basic nature of pyridinic N is conducive to HCHO adsorption [29,30]. Co@NC had a larger specific surface area and pore volume than Co-Co$_3$O$_4$@NC-30 (Table 2), which might endow Co@NC with better HCHO adsorption capacity. In addition to the specific surface area and doped pyridinic N contributing to HCHO surface adsorption, the intrinsic catalytic activity of the Co-based catalysts is critical for HCHO removal performance.

To assess the catalytic activity of the Co-based catalysts, the reaction product in the outlet gas was monitored. Fig. 4b shows the HCHO conversion rate and generated amounts of CO$_2$ over the catalysts; 88.9% of HCHO was converted into CO$_2$ using the Co@NC catalyst (calculated using Eq. (2)). The HCHO conversion rate exhibited by Co-Co$_3$O$_4$@NC-30 was significantly lower than that of Co@NC. The higher catalytic activity of Co@NC was probably due to its surface adsorption capability and intrinsic active sites. Firstly, the HCHO conversion rate
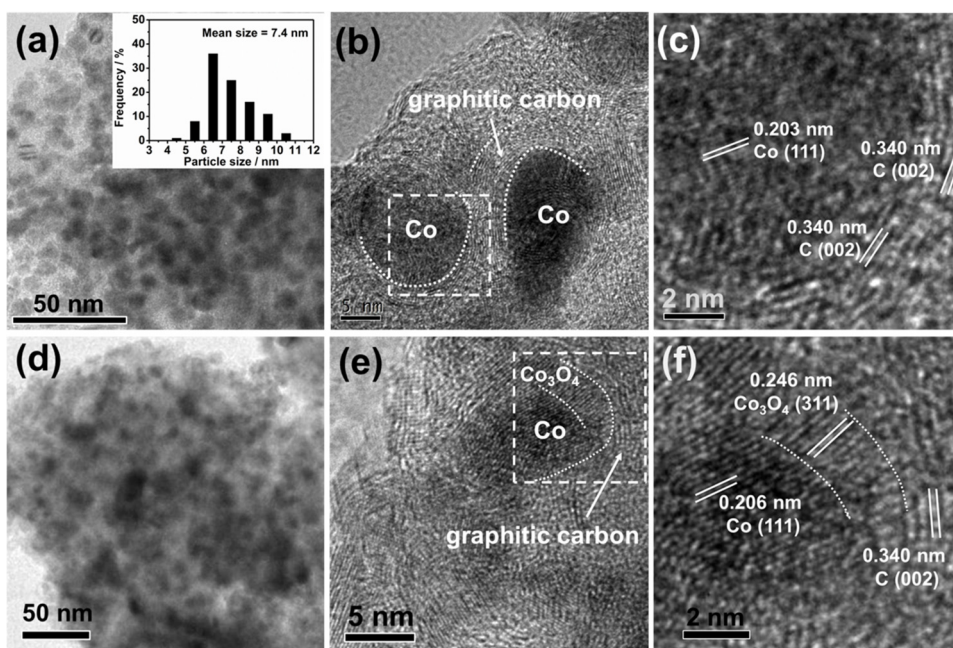
Fig. 2. TEM and HRTEM images of (a–c) Co@NC and (d–f) Co-Co$_3$O$_4$@NC-30. Panels (c) and (f) are enlarged images of (b) and (e), respectively. The inset in panel (a) shows the size distribution of Co NPs in Co@NC.

normalized by S_{BET} (X_{HCHO}') was calculated (as shown in Table 2) to evaluate the effect of the surface area. The X_{HCHO}' of Co@NC was clearly much larger than that of Co-Co$_3$O$_4$@NC-30, suggesting that the S_{BET} was not the dominant factor controlling the catalytic activity, although high surface area and porosity of Co@NC helped expose the active sites to reactants [15,46]. Secondly, the chemical composition of the catalysts is considered as this affects the intrinsic catalytic activity of the catalysts. Based on the results of physicochemical characterization, we confirmed that the metallic Co was partially oxidized and enfolded by Co$_3$O$_4$ in Co-Co$_3$O$_4$@NC-30. Considering that Co-Co$_3$O$_4$@NC was obtained from the oxidation of Co@NC under a mild oxidation process with little variation in the carbonaceous species, we concluded that transformation of metallic Co into Co$_3$O$_4$ and the subsequent

variation in the structure and chemical composition were the decisive factors reducing the catalytic activity of Co-Co$_3$O$_4$@NC-30.

The HCHO removal efficiency and conversion rate using Co@NC were approximately equal, while a distinct difference was observed for Co-Co$_3$O$_4$@NC-30 (Fig. 4a and b). Catalytic oxidation of HCHO is a heterogeneous reaction occurring at the gaseous HCHO/catalyst bi-phase boundary, where HCHO adsorption on the catalyst surface is the first step. The high surface area, large pore volume, hierarchical porous structure, and existence of pyridinic N all contributed to the porous carbon being a favorable support for HCHO adsorption and storage, facilitating the subsequent catalytic oxidation reaction. Therefore, the difference between the HCHO removal efficiency and conversion rate of Co-Co$_3$O$_4$@NC-30 was attributed to the incomplete catalytic oxidation
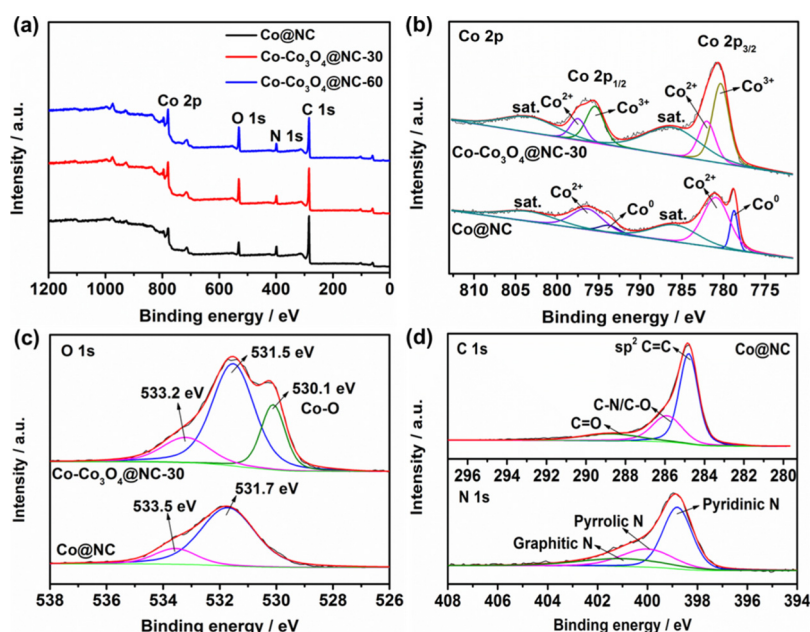

Fig. 3. XPS survey spectra (a) of Co@NC, Co-Co$_3$O$_4$@NC-30, and Co-Co$_3$O$_4$@NC-60; high-resolution Co 2p (b), O 1s (c), C 1s and N 1 s (d) spectra of the corresponding samples.

Table 1
Element contents of Co@NC and Co-Co$_3$O$_4$@NC measured by XPS.

Samples	Co (at.%)	Co^0 (at.%)	C (at.%)	O (at.%)	N (at.%)	Pyridinic N (at.%)
Co@NC	3.39	0.391	77.46	9.22	9.92	5.22
Co-Co$_3$O$_4$@NC-30	5.22	/	67.27	17.14	10.37	4.71

Table 2
BET surface area and pore volume of the two catalysts, along with their HCHO removal efficiency and conversion rate.

Sample	S_{BET}[a] (m$^2 \cdot$g^{-1})	Pore volume (cm$^3 \cdot$g^{-1})	η_{HCHO} (%)	X_{HCHO} (%)	X_{HCHO}[b] (% $\cdot$m$^{-2} \cdot$g)
Co@NC	291.3	0.176	85.6	88.9	0.305
Co-Co$_3$O$_4$@NC-30	177.0	0.130	51.4	32.5	0.184

[a] Specific surface area obtained from BET method.
[b] HCHO conversion rate normalized to S_{BET}.

of the adsorbed HCHO on the catalyst surface, with a portion of the gas adsorbed either as HCHO or as a transformed species in Co-Co$_3$O$_4$@NC-30. This phenomenon indicated that the metallic Co was the optimal active site for HCHO oxidation, rather than Co^{3+} in Co$_3$O$_4$.

To further investigate the adsorption and catalytic properties of porous carbon and metallic Co, the textural properties of NC and its long-term testing for HCHO removal was performed at identical conditions to those used when testing Co@NC. Both the BET specific surface area and pore volume of NC (Table S2) dramatically decreased after leaching of metallic Co, which was confirmed by XRD and TGA data (Fig. S8). We observed that the outlet concentration of HCHO increased rapidly and was similar to the initial concentration after 3 h, although HCHO was removed efficiently in the first few minutes (Fig. S9). In addition, the generated amount of CO$_2$ was quite low and gradually decreased to zero, suggesting that the catalytic activity was greatly degraded by the leaching of metallic Co. Therefore, the superior HCHO removal capability of Co@NC was attributed the metallic Co that served as active sites for HCHO oxidation. The contribution of NC for HCHO removal was further elucidated by comparing HCHO removal over Co$_3$O$_4$@NC and Co$_3$O$_4$. XRD and TGA were initially performed to authenticate their structures and compositions (Fig. S10). HCHO removal capability of Co$_3$O$_4$@NC and Co$_3$O$_4$ was extremely poor, and no CO$_2$ was generated (Fig. S11). The relative higher HCHO removal efficiency of Co$_3$O$_4$@NC compared with Co$_3$O$_4$ during the initial time was caused by HCHO adsorption in NC.

Recycling runs of HCHO removal was performed to evaluate the stability of Co@NC. Fig. 4c shows the removal efficiency slightly diminished after five-fold recycling, suggesting Co@NC possessed the outstanding stability. The long-term testing of HCHO removal furhter confirmed the stability of Co@NC (as shown in Fig. S12). XRD and XPS spectra also revealed there was no variation in structures and chemical compositions of the catalysts after HCHO oxidation reaction (as shown in Fig. S13). In addition, the effect of relative humidity (RH) on HCHO elimination was conducted (Fig. 4d). When the RH was increased from 25% to 50%, the HCHO removal efficiency remains 84%. Even under relative high RH (70%), ~80% of HCHO was removed, indicting Co@NC exhibited the excellent tolerability towards water vapor, revealing a great potential for practical applications.

3.3. Mechanism analyses

DFT calculations were performed to elucidate the roles of metallic Co as active sites for oxygen dissociation. p(3 × 3) supercell slabs were used for FCC Co (111) crystal facets with a 20 Å vacuum space, as shown in Fig. S14. During the calculations, three surfaces and the adsorbed species were fully relaxed. Four adsorption sites, including Top, Bridge, FCC and hexagonal close packed (HCP) sites, were present [47]. The potential energy profile of HCHO oxidation is shown in Fig. 5a. When HCHO and O$_2$ co-adsorbed on the Co (111) surface, O$_2$ dissociation via TS1 was facile, with an activation energy as low as 0.12 eV. In TS1, the O–O distance increased to 1.755 Å. The reaction energy was -2.56 eV, with two O atoms locating on two HCP sites with
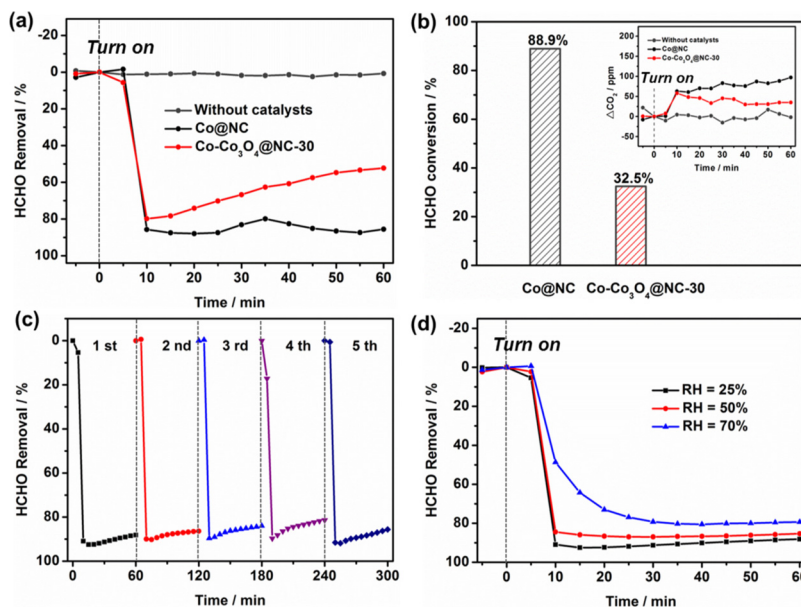
Fig. 4. (a) HCHO removal efficiency as a function of time and (b) HCHO conversion rates calculated after 60 min of testing over Co@NC and Co-Co$_3$O$_4$@NC-30 at room temperature with GHSV of 80,000 mL·(g·h)$^{-1}$. The inset shows the amount of CO$_2$ generated over the corresponding samples. HCHO removal efficiency as a function of time over Co@NC in five recycling runs (c) and under different RH (d). Reaction conditions: HCHO 100 ppm in air; total flow rate 100 mL·min^{-1}; RH ~25%.
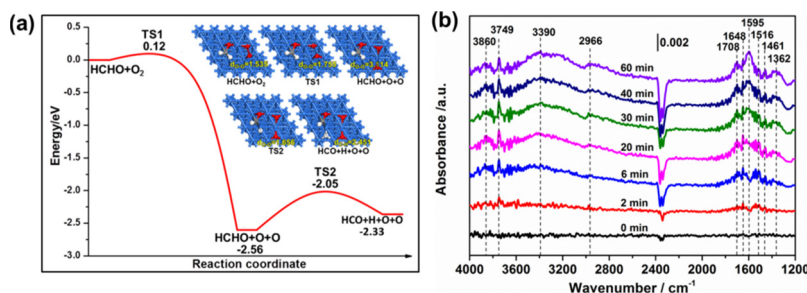
Fig. 5. (a) Potential energy profile of HCHO oxidation together with the structures of initial states, TSs and FSs on the Co(111) surface; (b) In situ DRIFTS spectra of O_2 + HCHO + N_2 gas mixture exposure for up to 60 min at room temperature over Co@NC diluted with KBr.
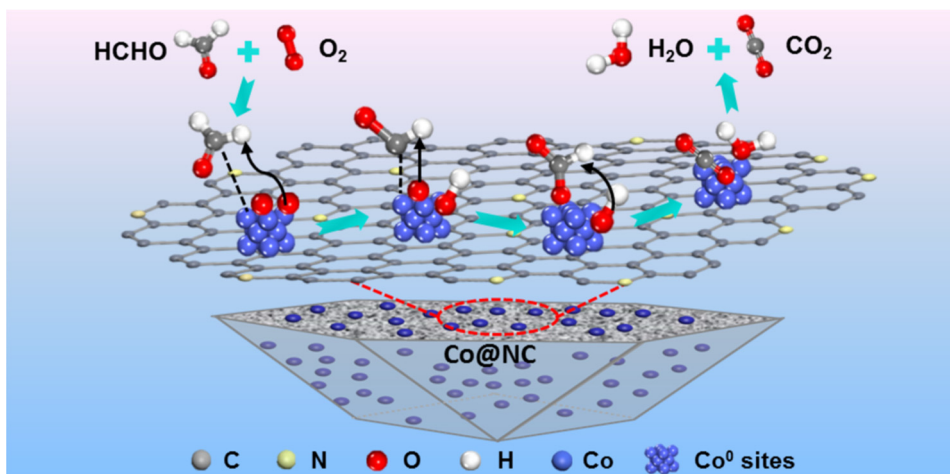

Fig. 6. Schematic illustration and reaction pathway of catalytic-oxidation of HCHO on the Co@NC catalyst at room temperature.

an O–O distance of 3.114 Å. HCHO dehydrogenation to HCO was also easy, with a low activation energy of 0.51 eV. The C–H distance increased to 1.656 Å in TS2 and 2.541 Å in final states (FS). The reaction was slightly endothermic, with a reaction energy of 0.23 eV.

In situ DRIFTS tests were performed to identify the intermediates in HCHO oxidation. Fig. 5b shows the DRIFTS spectra obtained after HCHO exposure for different times. Several peaks detected over the range of 3000–3860 cm^{-1} originated from the gradual accumulation of water molecules and hydroxyl groups [4,48]. The peaks at 1595 and 1362 cm^{-1} were assigned to asymmetric and symmetric COO$^-$ stretching vibrations of formate on the catalyst surface, while the band at 1708 cm^{-1} was attributed to the C=O group of COO$^-$, revealing that the formate species were the main intermediates during the oxidation process [48,49]. The peak at 1648 cm^{-1} was ascribed to water adsorbed on the catalyst, which was also observed in the spectra of pure KBr and originated from the moisture in the reactant gas [50] (Fig. S15). Based on the theoretical calculations and DRIFTS results, a schematic illustration and reaction mechanism for catalytic oxidation of HCHO is proposed, as shown in Fig. 6. HCHO and O_2 molecules were firstly adsorbed on Co@NC. Then, the adsorbed O_2 on the Co^0 surface split into active oxygen radicals and oxidized the adjacent HCHO to formate species. Then, the adsorbed formate species was further oxidized to adsorbed CO_2 and H_2O, which then desorbed from the Co surface.

4. Conclusions

Herein, carbon encapsulated Co-based catalysts were used for catalytic oxidation of HCHO at room temperature for the first time. The as-prepared Co@NC exhibited superior HCHO removal capacity and excellent catalytic activity for HCHO oxidation compared with Co-Co$_3$O$_4$@NC. The higher HCHO removal efficiency was attributed to its

larger surface area, hierarchically porous structure, higher pyridinic N contents, and especially the optimal metallic Co active sites for O_2 dissociation evidenced by DFT calculations. Transition-metal NP catalysts have great potential for HCHO elimination due to their superior removal capacity and low cost compared to noble-metal-based catalysts. Such materials are expected to contribute to the design of cost-effective catalysts for indoor air purification at room temperature.

Declaration of Competing Interest

The authors declare no competing financial interest.

Appendix A. Supplementary data

Supplementary material related to this article can be found, in the online version, at doi:https://doi.org/10.1016/j.apcatb.2019.117981.

References

[1] T. Salthammer, S. Mentese, R. Marutzky, Chem. Rev. 110 (2010) 2536–2572.
[2] C. Zhang, F. Liu, Y. Zhai, H. Ariga, N. Yi, Y. Liu, K. Asakura, M. Flytzani-Stephanopoulos, H. He, Angew. Chem. Int. Ed. 51 (2012) 9628–9632.
[3] X. Zhu, C. Jin, X.-S. Li, J.-L. Liu, Z.-G. Sun, C. Shi, X. Li, A.-M. Zhu, ACS Catal. 7

(2017) 6514–6524.

[4] J. Li, P. Zhang, J. Wang, M. Wang, J. Phys. Chem. C 120 (2016) 24121–24129.

[5] J. Ye, X. Zhu, B. Cheng, J. Yu, C. Jiang, Environ. Sci. Technol. Let. 4 (2016) 20–25.

[6] S. Suresh, T.J. Bandosz, Carbon 137 (2018) 207–221.

[7] J. Li, Xa. Dong, G. Zhang, W. Cui, Z. Wu, S.C. Lee, F. Dong, J. Mater. Chem. A 7 (2019) 3366–3374.

[8] Xa. Dong, W. Cui, H. Wang, J. Li, Y. Sun, H. Wang, Y. Zhang, H. Huang, F. Dong, Sci. Bull. 64 (2019) 669–678.

[9] X. Zhu, X. Gao, R. Qin, Y. Zeng, R. Qu, C. Zheng, X. Tu, Appl. Catal. B: Environ. 170–171 (2015) 293–300.

[10] X. Yang, X. Yu, M. Lin, M. Ge, Y. Zhao, F. Wang, J. Mater. Chem. A 5 (2017) 13799–13806.

[11] X. Tang, J. Chen, X. Huang, Y. Xu, W. Shen, Appl. Catal. B: Environ. 81 (2008) 115–121.

[12] Q. Xu, W. Lei, X. Li, X. Qi, J. Yu, G. Liu, J. Wang, P. Zhang, Environ. Sci. Technol. 48 (2014) 9702–9708.

[13] T. Yang, Y. Huo, Y. Liu, Z. Rui, H. Ji, Appl. Catal. B: Environ. 200 (2017) 543–551.

[14] C. Zhang, H. He, K.-i. Tanaka, Appl. Catal. B: Environ. 65 (2006) 37–43.

[15] B. Bai, H. Arandiyan, J. Li, Appl. Catal. B: Environ. 142 (2013) 677–683.

[16] J. Wang, P. Zhang, J. Li, C. Jiang, R. Yunus, J. Kim, Environ. Sci. Technol. 49 (2015) 12372–12379.

[17] Y. Huang, W. Fan, B. Long, H. Li, W. Qiu, F. Zhao, Y. Tong, H. Ji, J. Mater. Chem. A 4 (2016) 3648–3654.

[18] Z. Wang, W. Wang, L. Zhang, D. Jiang, Catal. Sci. Technol. 6 (2016) 3845–3853.

[19] L. Zhu, J. Wang, S. Rong, H. Wang, P. Zhang, Appl. Catal. B: Environ. 211 (2017) 212–221.

[20] Z. Dai, J. Su, X. Zhu, K. Xu, J. Zhu, C. Huang, Q. Ke, J. Mater. Chem. A 6 (2018) 14856–14866.

[21] Z. Fan, W. Fang, Z. Zhang, M. Chen, W. Shangguan, Catal. Commun. 103 (2018) 10–14.

[22] F. Liu, S. Rong, P. Zhang, L. Gao, Appl. Catal. B: Environ. 235 (2018) 158–167.

[23] C. Ma, D. Wang, W. Xue, B. Dou, H. Wang, Z. Hao, Environ. Sci. Technol. 45 (2011) 3628–3634.

[24] X.W. Xie, Y. Li, Z.Q. Liu, M. Haruta, W.J. Shen, Nature 458 (2009) 746–749.

[25] M. Huang, Y. Li, M. Li, J. Zhao, Y. Zhu, C. Wang, V.K. Sharma, Environ. Sci. Technol. 53 (2019) 3610–3619.

[26] M. Zhang, Q. Dai, H. Zheng, M. Chen, L. Dai, Adv. Mater. 30 (2018) 1705431.

[27] C. Zhang, X. Guo, Q. Yuan, R. Zhang, Q. Chang, K. Li, B. Xiao, S. Liu, C. Ma, X. Liu, Y. Xu, X. Wen, Y. Yang, Y. Li, ACS Catal. 8 (2018) 7120–7130.

[28] L. Lu, H. Tian, J.H. He, Q.W. Yang, J. Phys. Chem. C 120 (2016) 23660–23668.

[29] W. Liu, Y. Chen, H. Qi, L. Zhang, W. Yan, X. Liu, X. Yang, S. Miao, W. Wang, C. Liu, A. Wang, J. Li, T. Zhang, Angew. Chem. Int. Ed. 57 (2018) 7071–7075.

[30] X. Li, Y. Sun, T. Zhang, Y. Bai, X. Lyu, W. Cai, Y. Li, Nanotechnology 30 (2019) 105702.

[31] H. Chen, K. Shen, Q. Mao, J. Chen, Y. Li, ACS Catal. 8 (2018) 1417–1426.

[32] D. Luo, B. Chen, X. Li, Z. Liu, X. Liu, X. Liu, C. Shi, X.S. Zhao, J. Mater. Chem. A 6 (2018) 7897–7902.

[33] X.F. Zhu, J.G. Yu, C.J. Jiang, B. Cheng, Phys. Chem. Chem. Phys. 19 (2017) 6957–6963.

[34] D. Ding, K. Shen, X. Chen, H. Chen, J. Chen, T. Fan, R. Wu, Y. Li, ACS Catal. (2018) 7879–7888.

[35] Y. Liu, G. Han, X. Zhang, C. Xing, C. Du, H. Cao, B. Li, Nano Res. 10 (2017) 3035–3048.

[36] Z. Guo, F. Wang, Y. Xia, J. Li, A.G. Tamirat, Y. Liu, L. Wang, Y. Wang, Y. Xia, J. Mater. Chem. A 6 (2018) 1443–1453.

[37] Y.M. Chen, L. Yu, X.W. Lou, Angew. Chem. Int. Ed. 55 (2016) 5990–5993.

[38] H. Han, S. Chao, Z. Bai, X. Wang, X. Yang, J. Qiao, Z. Chen, L. Yang, ChemElectroChem 5 (2018) 1868–1873.

[39] M. Zhang, C. Wang, C. Liu, R. Luo, J. Li, X. Sun, J. Shen, W. Han, L. Wang, J. Mater. Chem. A 6 (2018) 11226–11235.

[40] A.T.E. Vilian, B. Dinesh, M. Rethinasabapathy, S.-K. Hwang, C.-S. Jin, Y.S. Huh, Y.-K. Han, J. Mater. Chem. A 6 (2018) 14367–14379.

[41] W. Ding, Z.D. Wei, S.G. Chen, X.Q. Qi, T. Yang, J.S. Hu, D. Wang, L.J. Wan, S.F. Alvi, L. Li, Angew. Chem. Int. Ed. 52 (2013) 11755–11759.

[42] D.H. Guo, R. Shibuya, C. Akiba, S. Saji, T. Kondo, J. Nakamura, Science 351 (2016) 361–365.

[43] G. Leofanti, M. Padovan, G. Tozzola, B. Venturelli, Catal. Today 41 (1998) 207–219.

[44] L. Nie, J. Yu, X. Li, B. Cheng, G. Liu, M. Jaroniec, Environ. Sci. Technol. 47 (2013) 2777–2783.

[45] L. Nie, J. Yu, M. Jaroniec, F.F. Tao, Catal. Sci. Technol. 6 (2016) 3649–3669.

[46] B. Bai, J. Li, ACS Catal. 4 (2014) 2753–2762.

[47] C. Chen, Q. Wang, G. Wang, B. Hou, L. Jia, D. Li, J. Phys. Chem. C 120 (2016) 9132–9147.

[48] F. Liu, J. Shen, D.F. Xu, W.Y. Zhou, S.Y. Zhang, L. Wan, Chem. Eng. J. 334 (2018) 2283–2292.

[49] J. Quiroz, J.-M. Giraudon, A. Gervasini, C. Dujardin, C. Lancelot, M. Trentesaux, J.-F. Lamonier, ACS Catal. 5 (2015) 2260–2269.

[50] R. Fang, H. Huang, J. Ji, M. He, Q. Feng, Y. Zhan, D.Y.C. Leung, Chem. Eng. J. 334 (2018) 2050–2057.